BEILSTEIN JOURNAL OF NANOTECHNOLOGY

Sonochemically assisted synthesis of metal-modified LTA zeolite/hydroxyapatite composites and their effect on microbial metabolic activity

Jesús Isaías De León-Ramírez[1], José Román Chávez-Méndez[2], Sergio Pérez-Sicairos[3], Lizzett López-Yee[1], Vitalii Petranovskii[4] and Víctor Alfredo Reyes-Villegas[*5]

Full Research Paper

Open Access

Address:
[1]Facultad de Odontología, Universidad Autónoma de Baja California, Calzada Universidad #14418, Parque Industrial Internacional Tijuana, 22424 Tijuana, B.C., México, [2]Facultad de Ciencias de la Salud Valle de las Palmas, Universidad Autónoma de Baja California, Blvd. Universitario 1000, Valle de las Palmas, 22260 Tijuana, B.C., México, [3]Centro de Graduados e Investigación en Química, Instituto Tecnológico de Tijuana, Cd. Industrial, 22444 Tijuana, B.C., México, [4]Centro de nanociencias y nanotecnología, Universidad Nacional Autónoma de México, Carr. Tijuana-Ensenada km 107, C.I.C.E.S.E., 22860 Ensenada, B.C., México and [5]Instituto de Investigaciones en Materiales, Universidad Nacional Autónoma de México, C.P.04510, Ciudad de México, México

Email:
Víctor Alfredo Reyes-Villegas[*] - victor.alfredo.reyes.villegas@uabc.edu.mx

* Corresponding author

Keywords:
hydroxyapatite composites; metabolic activity; metal zeolites; transition metals; ultrasonic synthesis

Beilstein J. Nanotechnol. **2026,** *17,* 1648–1662.
https://doi.org/10.3762/bjnano.17.114

Received: 08 July 2026
Accepted: 30 October 2026
Published: 20 November 2026

This article is part of the thematic issue: "Advances in the physics, chemistry, and applications of nanostructured materials".

Associate Editor: J. Lahann

© 2026 De León-Ramírez et al.; licensee Beilstein-Institut.
License and terms: see end of document.

Abstract

This preliminary study investigated the synthesis, characterization, and antimicrobial properties of metal-functionalized Linde Type A (LTA) zeolite/hydroxyapatite (HAp) composites prepared via a sonochemically assisted ion-exchange route. XRD, EDS, SEM, and UV–vis spectroscopy did not detect the formation of crystalline Ag, Zn, Fe, or Cu metal or oxide phases. Metal ions were proposed to be at different localizations, that is, Ag predominantly as surface nanoparticles, Zn as surface ions, and Fe/Cu primarily at cationic exchange sites. Agar diffusion assays showed no inhibition zones, indicating limited material diffusion. In contrast, broth microdilution assays revealed a concentration-dependent selective metabolic inhibition, inhibiting Gram-negative bacteria at lower concentrations (0.081 mg·mL^{-1}) and Gram-positive bacteria at higher concentrations (8.3 mg·mL^{-1}). Among the metal-containing samples, FeLTA@HAp demonstrated the most consistent broad-spectrum activity, achieving partial inhibition of metabolism in both Gram-positive and Gram-negative bacteria. These findings highlight the critical role of metal incorporation, surface distribu-

tion, and composite architecture in determining antimicrobial efficacy. This preliminary study shows the potential of the developed materials, particularly Fe-containing LTA@HAp, for future studies for use in biomedical applications such as infection-resistant bone grafts or implants with contact-active antimicrobial properties.

Introduction

Antimicrobial resistance (AMR) represents one of the most pressing global health threats of the 21st century [1]. In 2021, infections associated with resistant microorganisms were linked to approximately 4.71 million deaths, with projections estimating an increase to 8.22 million annual deaths by 2050 if current trends continue [2]. The consequences of AMR extend beyond the treatment of systemic infections and are particularly severe in the context of implant-associated infections. The use of implantable biomedical devices has expanded significantly in recent decades, with orthopedic and dental implants being the most prevalent in global clinical practice. Despite their proven efficacy, these devices carry an inherent risk of bacterial colonization and biofilm formation on their surfaces. Conventional antibiotic therapy is increasingly ineffective against biofilm-protected bacteria and further contributes to the selection of resistant strains [3,4]. Consequently, there is a strong demand for implantable materials that possess intrinsic antimicrobial properties while supporting tissue regeneration and osseointegration. In this context, functionalizing implant surfaces with antimicrobial materials has emerged as a promising strategy to prevent bacterial colonization directly at the implantation site, without relying exclusively on systemic or local antibiotic administration [4].

Among promising biomaterial platforms proposed for bone regeneration, composites based on zeolites and hydroxyapatite (HAp) have attracted considerable attention [5]. Zeolites are crystalline aluminosilicates characterized by a three-dimensional microporous architecture, high specific surface area, and exceptional ion-exchange capacity, enabling the incorporation of antimicrobial metal ions (Ag^+, Cu^{2+}, Zn^{2+}, $Fe^{2+/3+}$). These properties enable the incorporation and controlled release of metal ions with antimicrobial activity, while maintaining low systemic toxicity and adequate biocompatibility with mammalian tissues [6]. Previous studies have demonstrated that zeolite/HAp composites can enhance bone healing compared to individual components [7] and may serve as localized oxygen reservoirs, thereby improving the regenerative microenvironment.

Hydroxyapatite, due to its chemical and crystallographic similarity to the mineral phase of bone, exhibits outstanding osteoconductivity and biocompatibility, making it the benchmark inorganic coating for osteointegrative implants [7]. Beyond passive structural support, zeolites can contribute actively to the regenerative microenvironment by supplying oxygen to hypoxic peri-implant tissues and by modulating bone resorption, thereby creating favorable conditions for new bone formation. Functionalizing these composites with antimicrobial metal species further expands their therapeutic scope. The metals selected in this study act through complementary mechanisms [8]: Silver ions (Ag^+) disrupt the cell membrane, induce oxidative stress through reactive oxygen species (ROS), and interact directly with nucleic acids and key enzymatic proteins [9]; copper species (Cu^{2+}) promote microbial inactivation through contact-killing mechanisms [10]; zinc ions (Zn^{2+}) interfere with bacterial enzymatic activity and disrupt cellular metabolism [11]; and iron species (Fe^{2+}/Fe^{3+}) can generate ROS through Fenton-like reactions [12].

Zeolite/HAp composites have been prepared mainly by hydrothermal crystallization of HAp on the zeolite surface, by precipitation or sol–gel routes, or by mechanochemical mixing [5,13], and metal-exchanged Linde Type A (LTA) zeolite has been studied mostly in the form of single- or bimetallic systems at comparatively high loadings [14-16]. To our knowledge, Ag-, Zn-, Fe-, and Cu-modified LTA/HAp composites prepared under identical conditions have not been compared side by side, and a short, low-temperature sonochemical route has been applied neither to these composites. Ultrasound accelerates mass transfer and thereby enhances ion exchange and particle dispersion within minutes at low temperature [17], which helps to preserve both the LTA framework and the nanocrystalline HAp. The four metals chosen are among the most widely studied antimicrobial cations; they act through partly different pathways [10-12,18] and differ in toxicity, Zn and Fe being essential trace elements in bone. This preliminary study therefore aimed to establish whether the sonochemical route preserves the composite structure, and to screen the effect of the four selected metals on microbial metabolic activity in order to identify candidates for a subsequent optimization of metal and HAp loadings.

Experimental

Synthesis

All reagents were supplied by Sigma-Aldrich: $AgNO_3$ (Cat. No. 209139), $FeCl_3{\cdot}6H_2O$ (Cat. No. 236489), $CuSO_4{\cdot}5H_2O$ (Cat. No. 203165), $ZnCl_2$ (Cat. No. 208086), $NH_4H_2PO_4$ (Cat. No.

09721), $Ca(NO_3)_2$ (Cat. No. 239216), NaOH (Cat. No. 221465), $NaAlO_2$ (Cat. No. 13404), and $Na_2O(SiO_2)_x{\cdot}xH_2O$ (Cat. No. 338443). Ultrasonic energy was delivered with a Branson sonifier of the SLP series (SLPt, 150 W, 40 kHz) fitted with a tapered 1/8″ microtip, operated at 30% amplitude in continuous mode.

LTA zeolite was synthesized by a hydrothermal method based on the procedure of Thompson and Franklin [19], with slight modifications of the precursors (NaOH, $NaAlO_2$, and $Na_2O(SiO_2)_x{\cdot}xH_2O$). First, 7.23 g of NaOH was dissolved in 2 L of deionized water in a polypropylene bottle under gentle stirring. Then, 165.16 g of $NaAlO_2$ was added and the mixture was stirred until a clear solution was obtained. Next, 2 L of a commercial sodium silicate solution was poured into the aluminate solution, forming a viscous gel. The container was sealed tightly and shaken manually until the gel was uniform. The gel was then crystallized hydrothermally at 99 ± 1 °C for 4 h under static conditions. After crystallization, the suspension was allowed to cool to room temperature (<30 °C), and the solid product was recovered by decantation. The solid was washed with an excess of deionized water until the supernatant reached pH < 9, filtered under vacuum through a 0.45 µm nitrocellulose membrane with excess rinse water, and dried in an oven at 80 °C overnight [18].

HAp was synthesized by an ultrasound-assisted method. A solution of 0.29 M $NH_4H_2PO_4$ and 0.24 M $Ca(NO_3)_2$ was reacted at pH 11 and 5 °C under ultrasound for 30 min. The white suspension obtained was centrifuged, and the solid was filtered under vacuum through a 0.45 µm nitrocellulose membrane with excess rinse water, dried in an oven at 90 °C overnight, and then dried in a furnace at 150 °C for 12 h. The resulting material was used for the modification of LTA.

The modification of LTA was carried out in three steps, that is, sonication in the presence of the metal precursor, drying, and sonication with HAp. All ultrasonic treatments were performed under continuous sonication at 30% amplitude, with the reaction temperature maintained at 5 °C, and the sonication time was fixed at 5 min for every step. For the preparation of the metal-exchanged zeolites, 5 g of Na-LTA was dispersed in 50 mL of deionized water, and 121.7 µL of a 0.05 M aqueous solution of the corresponding metal precursor (Ag^+, Zn^{2+}, Fe^{3+}, or Cu^{2+}) was added, corresponding to a metal-to-LTA molar ratio of 0.002. The mixture was sonicated for 5 min at 5 °C and dried at 150 °C for 3 h. The materials obtained were designated AgLTA, FeLTA, ZnLTA, and CuLTA. For the composites, 5 g of each zeolitic material was redispersed in 50 mL of deionized water and mixed with 0.1529 g of HAp, corresponding to a HAp-to-LTA molar ratio of 0.05. The suspensions were sonicated again under identical conditions (30% amplitude, 5 °C, 5 min) and dried at 150 °C for 3 h. The library evaluated in this preliminary study consisted of seven samples, namely, pristine LTA, pure HAp, the metal-free LTA@HAp composite, and the four metal-containing composites (AgLTA@HAp, ZnLTA@HAp, FeLTA@HAp, and CuLTA@HAp). This set was chosen to establish the individual and combined contributions of LTA, HAp, and metal incorporation to the physicochemical, optical, and antibacterial properties of the composites before a larger optimization study with variable metal and HAp loadings. Likewise, for this work, the term composite denotes a two-phase material, in which pre-formed nanocrystalline HAp is physically associated with the surface of the LTA crystals. No chemical reaction between the aluminosilicate framework and the hydroxyapatite is expected under the conditions used and no new phase or compound is claimed.

Characterization

X-ray diffraction patterns were recorded in 0.01° steps in 2θ over the 6–80° range using Cu Kα radiation (λ = 1.5406 Å). Micrographs were obtained with a JEOL JIB-4500 (SEM+FIB) equipped with energy-dispersive X-ray spectroscopy (EDS) at an accelerating voltage of 20 kV. Chemical formulae were derived from the EDS data by converting atomic percentages into moles, with the water content estimated from the oxygen not assigned to the LTA framework $Na_{12}Al_{12}Si_{12}O_{48}{\cdot}27H_2O$. UV–vis spectra were recorded from 230 to 1000 nm with an EnSpire multiplate reader, using 200 µL of the material suspension per well (optical path 0.53 cm). The optical bandgap (E_g, eV) was obtained from a linear fit over the 4.1–4.5 eV interval of the Tauc plot, $(\alpha h\nu)^{1/n}$ vs $h\nu$, for the direct allowed, direct forbidden, indirect allowed, and indirect forbidden models, by extrapolating the fitted line to the abscissa, where:

$$\alpha = \text{absorption coefficient}\left(\alpha = \frac{\ln 10 \cdot A}{d}\right). \tag{1}$$

Here, A is the absorbance, d the photon path length, h the Planck constant, ν the light frequency, and n indicates the transition type, that is, n = 1/2 (direct allowed), n = 3/2 (direct forbidden), n = 2 (indirect allowed), or n = 3 (indirect forbidden). The bandgap was calculated from the parameters of the linear fit as:

$$E_g = \frac{-\text{Intercept}}{\text{Slope}}. \tag{2}$$

The transition model used for the E_g shift was the one for which $R^2 > 0.9$ and $E_g > 1$ eV, which was taken as the most physically realistic value.

Antimicrobial activity

The antimicrobial activity of the synthesized materials was evaluated against reference strains from the American Type Culture Collection (ATCC®): *Escherichia coli* ATCC® 25922, *Pseudomonas aeruginosa* ATCC® 27853, *Enterococcus faecalis* ATCC® 29212, *Staphylococcus aureus* ATCC® 25923, and *Staphylococcus epidermidis* ATCC® 12228; the fungal strains were *Candida albicans* ATCC® 10231 and *Candida parapsilosis* ATCC® 90112. Before testing, all microorganisms were cultured in the corresponding medium (Mueller–Hinton broth for bacteria and Sabouraud broth for fungi) until the turbidity was equivalent to a 0.5 McFarland standard. The inoculum density was adjusted by measuring the optical density at 620 nm. All experiments were performed in triplicate.

To establish whether the antimicrobial activity of the modified LTA zeolite warranted further study, the materials were first compared with a panel of antibiotics against a buccal sample obtained by swabbing the oral cavity. Samples were collected from adult volunteers at Albergue Las Memorias. The study was approved by the Research Ethics Committee of Albergue Las Memorias A.C., all participants gave written informed consent before the buccal sample was collected, and all methods were performed in accordance with the relevant guidelines and regulations. For this test, the powder was placed at the center of the agar plate and the antibiotic discs at the periphery (Figure 1A).

Once the materials had been confirmed to be of interest, their antimicrobial activity was screened against the ATCC strains of *E. coli*, *E. faecalis*, *S. aureus*, *P. aeruginosa*, *C. albicans*, and *C. parapsilosis* by the agar diffusion method (Figure 1B). Suspensions adjusted to a 0.5 McFarland standard were spread onto Mueller–Hinton agar plates for the bacterial strains and onto Sabouraud agar plates for the fungal strains. The powdered materials were dispersed in sterile water at 1 mg·mL^{-1}, and sterile paper discs impregnated with the corresponding suspension were placed on the inoculated agar surface. The plates were incubated aerobically at 37 °C for 24 h, after which antimicrobial activity was assessed by visual inspection of the inhibition zones. Differences in antimicrobial performance were used as an indirect indicator of the incorporation and bioavailability of the metal species within the zeolitic framework.

A second antimicrobial experiment was performed by broth microdilution. From a freshly adjusted 0.5 McFarland suspension of *E. coli*, *P. aeruginosa*, *E. faecalis*, *S. aureus*, and *S. epidermidis*, 100 µL was transferred to 100 µL of fresh sterile medium in a 96-well microplate, followed by 20 µL of a zeolitic suspension (1, 10, 25, 50, or 100 mg·mL^{-1}), giving final well concentrations of, respectively, 0.08, 0.8, 2.1, 4.2, and 8.3 mg·mL^{-1}. The microplates were incubated at 37 °C for 48 h, after which they were transferred to a laminar-flow hood, and 20 µL of sterile resazurin solution was added to each well. The plates were incubated at 37 °C for 1 h to allow the color to change, and fluorescence was then measured for each well in an EnSpire multiplate reader with excitation at 560 nm and emission at 590 nm. Each sample had its own positive control (C+, the corresponding antibiotic) and negative control (C−, 20 µL of sterile broth instead of the zeolitic suspension). A blank with-

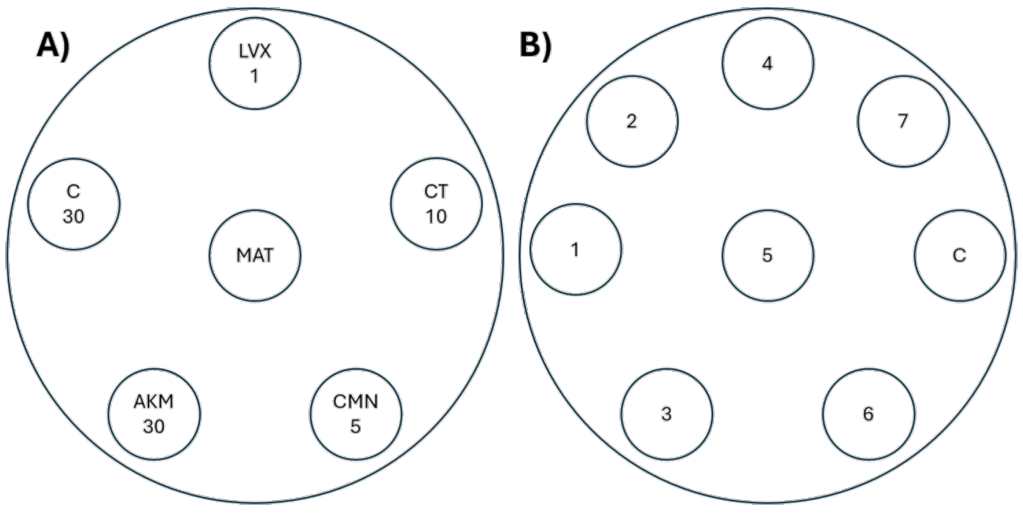

Figure 1: Layout of the agar diffusion assay. (A) Antibiotic susceptibility controls and placement of the powdered material (MAT). Antibiotic discs: LVX1, levofloxacin (1 µg); C30, chloramphenicol (30 µg); CT10, colistin (10 µg); AKM30, amikacin (30 µg); CMN5, cefminox (5 µg). (B) Distribution of the tested materials: (1) LTA, (2) HAp, (3) LTA@HAp, (4) ZnLTA@HAp, (5) CuLTA@HAp, (6) FeLTA@HAp, (7) AgLTA@HAp. (C) Corresponding negative control for each bacterial strain.

out bacteria was also measured to confirm that the zeolite did not interact with the culture broth or with resazurin. All experiments were performed in triplicate and analyzed by three-way ANOVA, with metabolic activity (%) as the response and Gram classification (Gram− or Gram+), material (HAp, LTA, LTA@HAp, FeLTA@HAp, AgLTA@HAp, CuLTA@HAp, and ZnLTA@HAp) and final well concentration (0.08, 0.8, 2.1, 4.2, and 8.3 mg·mL^{-1}) as factors.

Metabolic activity was calculated for every material-strain-concentration combination as:

$$\text{Metabolic Activity}(\%) = \left(\frac{\text{Sample}}{\text{C}-}\right) \times 100, \qquad (3)$$

where C− is the untreated negative control. On the basis of the metabolic activity, each combination was classified as inactive (metabolic activity > 50%), partial metabolic inhibitor (11–50%), or strong metabolic inhibitor (≤10%).

Results and Discussion

Characterization

The X-ray diffraction results (Figure 2) confirm the characteristic cubic structure of the LTA zeolite, identified by its principal reflections at approximately 7.2°, 10.2°, 12.5°, 16.1°, and 21.7° in 2θ (COD 7117433). The pattern of the reference HAp shows broad, low-intensity peaks, characteristic of a poorly crystalline or nanocrystalline hydroxyapatite, in agreement with previous reports for synthetic HAp [20]. All composites retained the characteristic cubic morphology of the LTA zeolite and its high crystallinity, as shown by the XRD patterns and the Rietveld refinement. The absence of additional reflections from metal oxides or metallic phases, together with the minor shifts of the diffraction peaks, indicates that Ag, Cu, Zn, and Fe may be incorporated as extra-framework cations or as highly dispersed surface species. However, the low metal contents used (molar ratio Me/LTA = 0.002) are difficult to detect by XRD. The same limitation applies to HAp; even though a higher amount was used (HAp-to-LTA molar ratio of 0.05), its broad reflections are difficult to resolve by this technique. SEM confirmed these observations, showing no visible metal aggregates, and EDS confirmed the presence of HAp through the increased P and Ca contents. These results are consistent with the mild conditions of the ultrasound-assisted synthesis, which prevented framework collapse and excessive dealumination.

After the incorporation of hydroxyapatite (LTA@HAp) and the subsequent incorporation of the metal cations (AgLTA@HAp, ZnLTA@HAp, FeLTA@HAp, and CuLTA@HAp), the diffraction patterns fully preserved the characteristic peaks of the LTA zeolite; there was no evidence of new crystalline phases or of secondary metal oxides such as CuO, ZnO, or Fe_2O_3, or of metallic Ag^0. This suggests that the metals are well dispersed, possibly as small clusters within the zeolitic network, rather than as a segregated crystalline phase on the surface [14,15,21,22].

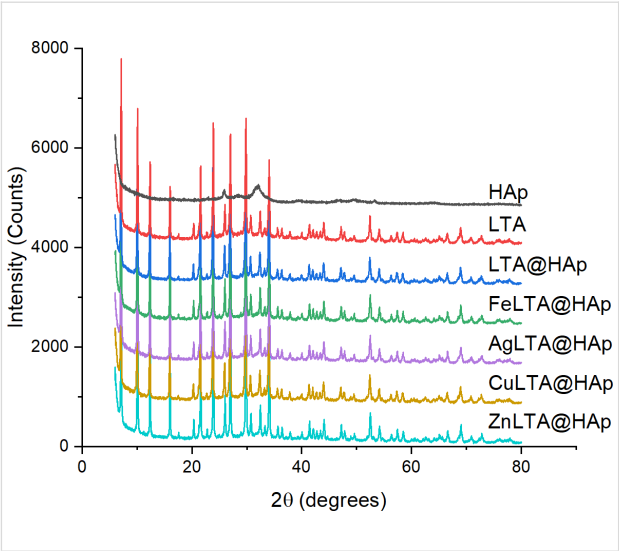

Figure 2: X-ray diffraction patterns of HAp, LTA zeolite, and the composites LTA@HAp, AgLTA@HAp, ZnLTA@HAp, FeLTA@HAp, and CuLTA@HAp.

Slight shifts towards smaller cell parameters were nevertheless observed for the LTA zeolites after metal incorporation, which suggests a contraction of the unit cell. This can be attributed to the replacement of the charge-compensating Na^+ (ionic radius 1.02 Å) by cations of different size, such as Ag^+ (1.15 Å), Zn^{2+} (0.74 Å), Fe^{2+} (0.78 Å), and Cu^{2+} (0.73 Å) [18,23], and to differences in electron affinity, which generate an elastic distortion of the SiO_4/AlO_4 tetrahedra that constitute the zeolitic framework [18]. Despite these shifts, the microstrain and the relative crystallinity of the composites changed only slightly, by 0.029% and 16.80%, respectively. This is evidenced by the preservation of the resolution and intensity of the principal diffraction peaks, which confirms that neither the metals nor the HAp decoration compromises the structural integrity of the LTA zeolite.

The HAp was found to consist of nanocrystals of ≈9 nm (Table 1), and its concentration was too low to be detected reliably by XRD. Further analyses are therefore needed to confirm the presence of both HAp and the metals in the modified zeolite and to elucidate the location and coordination of the metals. This may be difficult, or even impossible, at the low molar ratios used with the techniques and resolutions currently available.

Table 1: Structural and fit quality parameters obtained by Rietveld refinement for HAp, LTA zeolite, and the composite materials LTA@HAp, CuLTA@HAp, AgLTA@HAp, ZnLTA@HAp, and FeLTA@HAp.

	Cell parameter *a* (Å)	Microstrain (%)	Crystallite size (nm)	Crystallinity (%)	GOF	R_p	R_{wp}	R_{Bragg}
HAp	9.54	1.043	6.13	50.57	4.29	13.53	16.64	7.4496
LTA	24.66	0.148	85.68	100	2.21	6.91	9.12	0.0014
LTA@HAp	24.64	0.145	73.08	115.62	1.84	6.49	8.64	0.0020
CuLTA@HAp	24.64	0.145	77.38	116.80	2.18	7.10	9.39	0.0071
AgLTA@HAp	24.62	0.146	95.49	116.09	2.25	7.24	9.51	0.9638
ZnLTA@HAp	24.63	0.116	112.01	114.91	2.21	7.17	9.28	0.0041
FeLTA@HAp	24.62	0.119	93.85	114.35	2.01	6.75	8.85	0.9561

SEM (Figure 3) shows the morphological evolution of the materials through the synthesis. The HAp consists of aggregates of small spherical particles with a marked tendency to agglomerate, typical of nanocrystalline HAp [24]. Pure LTA zeolite exhibits the well-defined cubic morphology characteristic of this structure, with angular edges, smooth surfaces and a homogeneous size distribution in the micrometer range, consistent with the XRD data and with previous reports [18].

In LTA@HAp (Figure 3C), the cubic zeolite crystals retain their original geometry [18]. The HAp content of the composites is 2.97 wt %. For LTA crystals of 1–2 µm, whose external surface area is of the order of 1.5–3.0 $m^2 \cdot g^{-1}$, this corresponds to an equivalent layer of only 3–6 nm, or to a partial coverage of the external surface by the ≈9 nm crystallites identified by XRD. Features of this size cannot be resolved with the conventional SEI detector and the magnifications used here. These micrographs and the EDS analyses presented in this work establish the presence and the bulk proportion of the two phases; but they do not resolve the HAp nanocrystals individually and do not localize them on specific crystal faces. Whether the apatite is attached to the external surface of the zeolite crystals or is present as a finely dispersed separate phase was not established. Field-emission SEM at high magnification with low-voltage EDX mapping, or STEM-EDS on dispersed particles, is required to distinguish between these two situations and will be performed in the follow-up study.

The addition of metals (Figure 3D–G) likewise preserves the morphology of the LTA zeolite, with no visible segregated metal particles or oxide deposits on the surface. For example, among the metal-containing samples, ZnLTA@HAp with the largest crystallite size obtained by Rietveld refinement (112.01 nm), and CuLTA@HAp with the smallest (77.38 nm), both show well-defined cubic crystals with a rough surface that may be due to the HAp coating. The EDS analysis (Table 2) complements the morphological and crystallographic results. Pure LTA has a Si/Al ratio of 0.993, close to the theoretical

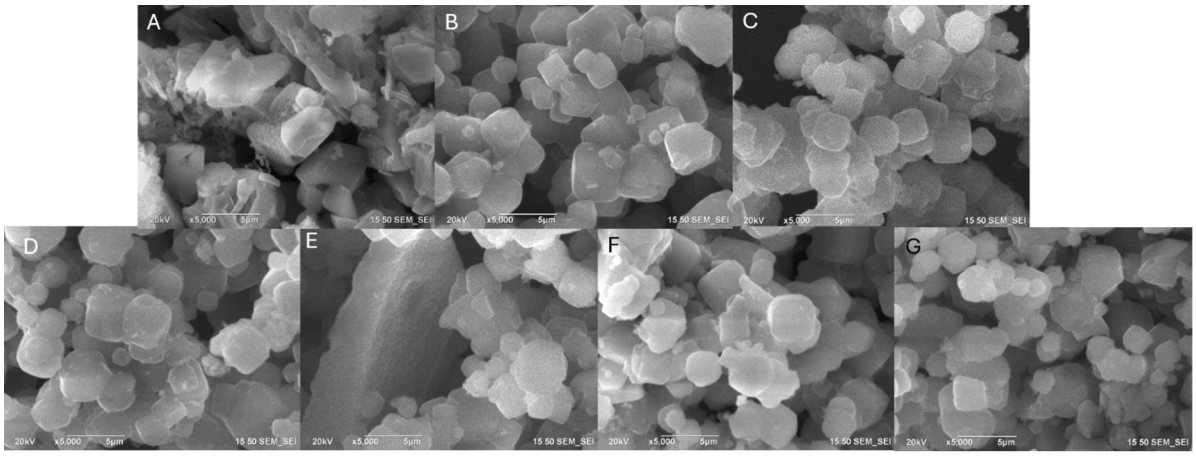

Figure 3: Scanning electron microscopy (SEM) micrographs of: (A) HAp, (B) LTA, (C) LTA@HAp, (D) FeLTA@HAp, (E) AgLTA@HAp, (F) CuLTA@HAp, and (G) ZnLTA@HAp. The images were obtained at an accelerating voltage of 20 kV with SEI detectors; scale bars: 5 µm.

Table 2: Atomic percentage elemental composition (EDS), normalized chemical formula, and Si/Al Ratio of LTA zeolite, HAp, and composite materials LTA@HAp, AgLTA@HAp, ZnLTA@HAp, FeLTA@HAp, and CuLTA@HAp.

Sample	Elemental fraction [atom %]						Chemical formula	Si/Al
	O	Na	Al	Si	P	Ca		
LTA	64.8	12.5	11.4	11.3	0	0	$Na_{13.3}[Al_{12.1}Si_{12}O_{48}]\cdot 20.830H_2O$	1.0
HAp	71.7	0	0.26[a]	0.1[a]	16.31	11.6	$Ca_{0.71}(PO_4)_1(OH)_{1.58}$	–
LTA@HAp	65.13	11.7	10.81	10.72	0.7	0.94	$\|Ca_{0.09}(PO_4)_{0.07}(OH)_{0.02}\|Na_{13.1}[Al_{12}Si_{12}O_{48}]\cdot 24.42H_2O$	1.0
AgLTA@HAp	65.45	11.57	10.62	10.79	0.68	0.88	$\|Ca_{0.08}(PO_4)_{0.06}(OH)_{0.03}\|Na_{13}[Al_{12}Si_{12}O_{48}]\cdot 24.89H_2O$	1.0
ZnLTA@HAp	65.42	11.69	10.37	10.35	1	1.18	$\|Ca_{0.11}(PO_4)_{0.10}(OH)_{0.06}\|Na_{13}[Al_{12}Si_{12}O_{48}]\cdot 27.35H_2O$	1.0
FeLTA@HAp	65.84	11.7	10.37	10.3	0.88	0.92	$\|Ca_{0.09}(PO_4)_{0.09}(OH)_{0.08}\|Na_{13}[Al_{12}Si_{12}O_{48}]\cdot 28.12H_2O$	1.0
CuLTA@HAp	65.58	11.91	10.46	10.7	0.65	0.7	$\|Ca_{0.07}(PO_4)_{0.06}(OH)_{0.05}\|Na_{13}[Al_{12}Si_{12}O_{48}]\cdot 25.79H_2O$	1.0

[a]Values below approximately 0.3 atom % are at the limit of quantification of the EDS analysis and are reported as <LOQ; they are not used for any ratio.

value of the unit cell of zeolite A (Si/Al ≈ 1) [18]. HAp shows the characteristic elements O, P, and Ca, corresponding to a calcium-deficient, non-stoichiometric hydroxyapatite, $Ca_{10-x}(HPO_4)_x(PO_4)_{6-x}(OH)_{2-x}$ [25]. The preparation was not compared with an otherwise identical procedure performed without ultrasound. Such a control is required to attribute the dispersion of the HAp and the degree of metal exchange to the ultrasonic treatment rather than to mixing alone, and it is included in the design of the optimization study.

In the LTA@HAp and MeLTA@HAp materials, the elements of both phases are present (Na, Al and Si from the zeolite and P and Ca from the HAp), and the Si/Al ratio remains close to unity in all cases (0.991–1.023, Table 2), confirming that neither the metal addition nor the HAp coating alters the stoichiometry of the aluminosilicate framework and that no dealumination occurred during the treatments [14]. Metal signals were not detected by EDS in any composite, which is expected because the nominal metal content (<0.01 wt %) is below the detection limit of the technique. A further possibility that cannot be excluded with the present data is that part of the metal is associated with the apatite rather than with the zeolite. Hydroxyapatite readily incorporates divalent and transition-metal cations by substitution at the Ca sites and by surface complexation, and a redistribution of this kind could occur during the second sonication step, although the exchange was performed on Na-LTA before the HAp was added. Because the metal contents are below the detection limits of both XRD and EDS, the partition of the metals between the two phases was not determined. The slightly lower Na content of all composites relative to pristine LTA (11.6–11.9 atom % vs 12.5 atom %) is also observed for the metal-free LTA@HAp (11.7 atom %) and is therefore attributed to dilution by HAp rather than to Na^+/Me^{n+} exchange (Table 2). EDS thus confirms the presence of HAp, through the increase in P (0.65–1.00 atom %) and Ca (0.70–1.18 atom %) relative to pure LTA (P and Ca, 0 atom %) in all the synthesized materials.

Pure LTA zeolite and HAp showed low absorption over the whole measured range (Figure 4A), consistent with their wide bandgap and with the absence of chromophoric centers in their frameworks [18,26]. This behavior agrees with the crystallographic data, which showed well-ordered LTA and nanocrystalline HAp free of metallic impurities. The incorporation of HAp on the zeolite surface (LTA@HAp) produced only a marginal increase in absorbance, confirming that the optical response of the support is dominated by the zeolitic framework. In contrast, the spectra of all metal-containing composites changed in a metal-dependent manner around 350 nm, showing that the transition metals introduce new electronic states that extend the optical response. According to the EDS data, this response cannot be attributed to framework degradation since the Si/Al stoichiometry of ≈1 is preserved, which suggests that the optical changes arise from the interaction of the metals with the zeolitic framework.

The Ag-containing composite showed an additional band in the 300–450 nm region, where the localized surface plasmon resonance of Ag clusters or of partially reduced Ag^0 species is typically observed in zeolite channels [27]. This is notable because the XRD patterns showed no reflections of metallic Ag^0, which suggests that the plasmonic species are present as sub-nanome-

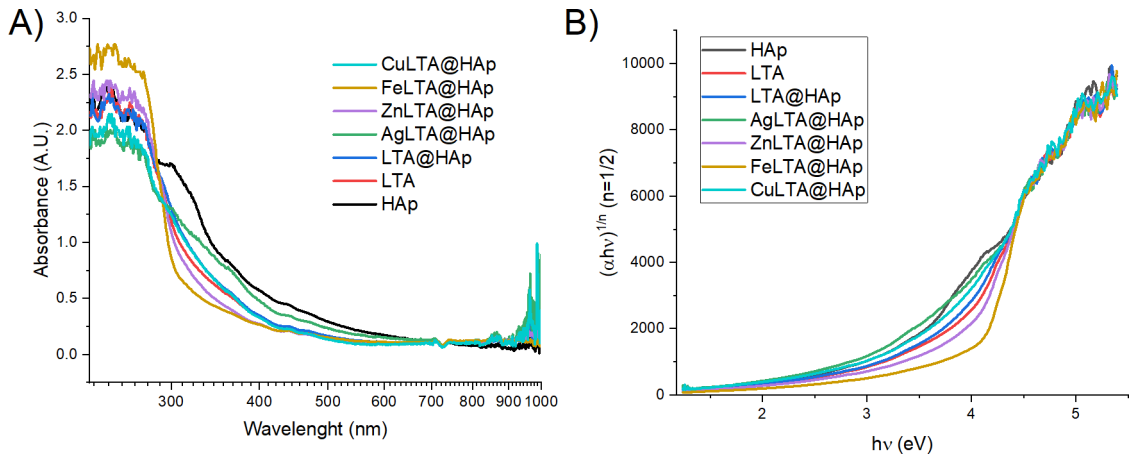

Figure 4: (A) UV–vis spectra and (B) Tauc plots of LTA, HAp, and metal-modified LTA@HAp composites (Ag, Zn, Fe, and Cu) for the determination of optical bandgap energy using a direct allowed (n = 1/2) electronic transition model.

ter clusters below the XRD detection limit, a well-documented phenomenon in Ag-zeolite systems [28]. The Zn- and Cu-containing samples showed smaller changes, suggesting that their optical contributions are associated mainly with ligand-related processes and with perturbations of the zeolitic electronic structure [29]. Taken together, XRD (no metal or oxide reflections), EDS (no segregated metal signals), and the UV–vis features point to highly dispersed metal species whose probable location differs from element to element. The lower absorbance of the Zn sample in the same region is consistent with predominantly ionic surface species [18], and the absorption below 300 nm for Fe and Cu is consistent with mononuclear cationic species at exchange sites [30]. We emphasize that UV–vis spectroscopy cannot establish surface versus framework localization, that these assignments should be regarded as a proposed speciation rather than proof, and that they would benefit from confirmation by XPS or X-ray absorption spectroscopy on samples with higher metal contents.

The optical properties of the materials (Figure 4B) were evaluated by Tauc analysis using four electronic-transition models, namely, direct allowed (n = 1/2), direct forbidden (n = 3/2), indirect allowed (n = 2), and indirect forbidden (n = 3) (Table 3). The estimated bandgaps confirm that pristine LTA and HAp have wide bandgaps, consistent with their nature as UV-active insulating materials with a limited response to visible light [31]. The incorporation of metal ions modified the optical gap in a metal-dependent manner, which is

Table 3: Parameters obtained from the Tauc analysis for HAp, LTA, LTA@HAp, AgLTA@HAp, ZnLTA@HAp, FeLTA@HAp, and CuLTA@HAp, considering the models of direct allowed (n = 1/2), direct forbidden (n = 3/2), indirect allowed (n = 2), and indirect forbidden (n = 3) electronic transitions.

Models	LR	HAp	LTA	LTA@HAp	AgLTA@HAp	ZnLTA@HAp	FeLTA@HAp	CuLTA@HAp
direct allowed (n = 1/2)	m	4124.4	7332.6	6738.1	4913.6	8761.8	12204.6	5806
	E_g	3.13	3.71	3.63	3.35	3.83	4.02	3.5
	R^2	0.9194	0.9915	0.9869	0.9464	0.9947	0.9935	0.9602
direct forbidden (n = 3/2)	m	4.8	9.3	8.2	5.8	11.5	16.9	6.9
	E_g	0.75	2.54	2.29	1.41	2.92	3.42	1.88
	R^2	0.9352	0.9965	0.9946	0.962	0.9982	0.9969	0.976
indirect allowed (n = 2)	m	1.8	3.5	3.1	2.1	4.3	6.5	2.6
	E_g	−0.44	1.96	1.62	0.45	2.46	3.13	1.07
	R^2	0.9371	0.9966	0.995	0.9637	0.9978	0.9968	0.9777
indirect forbidden (n = 3)	m	0.6	1.2	1	0.7	1.5	2.2	0.8
	E_g	−2.89	0.8	0.29	−1.48	1.55	2.55	−0.54
	R^2	0.9389	0.9965	0.9954	0.9654	0.9972	0.9965	0.9793

[a]LR are the linear regression parameters ($y = mx + b$), for slope (m), bandgap energy (E_g, eV), and correlation coefficient (R^2).

consistent with the formation of intra-bandgap states associated with the d-orbital contributions of the transition metals [32]. The indirect models (n = 2 and 3) produced less well-defined linear regions, suggesting that phonon-assisted transitions are not the dominant optical mechanism in these materials [33].

The extracted E_g values (Figure 5) change in the following order: FeLTA@HAp > ZnLTA@HAp > LTA > LTA@HAp > CuLTA@HAp > AgLTA@HAp > HAp. Pristine LTA and HAp show wide optical gaps (direct allowed, E_g = 3.71 and 3.13 eV, respectively), consistent with their character as UV-active insulators with a limited visible-light response [31]. The metal cations modified the gap in a metal-dependent manner: Ag and Cu narrowed it (E_g = 3.35 and 3.50 eV, respectively), consistent with the introduction of intra-bandgap states arising from their d-orbital contributions [32], whereas Fe and Zn widened it relative to LTA@HAp (E_g = 4.02 and 3.83 eV, respectively). This behavior mirrors the absorbance data, that is, a pronounced 300–450 nm feature for Ag, weaker perturbations for Cu, and higher-energy absorption (<300 nm) for Fe; it may indicate that the cations differ both in electronic perturbation and in localization, rather than acting through a single common mechanism. The direct allowed model was chosen for the determination of E_g because it gave the most linear Tauc regions (R^2 > 0.9) and physically meaningful gaps (E_g > 1 eV), whereas the indirect models (n = 2 and 3) gave poorly defined linear regions and, in several cases, unphysical negative intercepts [33].

The characterization shows that no crystalline metal phase is present (XRD) and that the metals are not aggregated into larger particles (SEM), which is supported by the EDS data. The metals may therefore be highly dispersed throughout the material, producing the small, element-specific changes observed in the UV–vis spectra. These changes may also help to explain their roles in the antimicrobial behavior, such as contact-mediated effects and physical adsorption.

Antibacterial activity

The antimicrobial activity depended strongly on the test method, the composition of the material, the concentration, and the target microorganism. The complete absence of inhibition zones in the agar diffusion assays, for every material and strain, indicates that any diffusible metal release was below the level needed to produce an antimicrobial effect, and points to contact-dependent mechanisms rather than to classical ion-release activity. In the assay against the buccal swab (Figure 6), no inhibition halos were observed for any of the samples; microorganisms grew in the vicinity of most discs, and only cefminox (CMN) produced a clear zone.

In the assays against the ATCC strains (Figure 7), no inhibition zones were observed for any sample or strain. Rather than demonstrating a complete absence of ion release, this is most consistent with a diffusive metal release below the threshold required for zone formation, which is expected at the low nominal metal loading used (molar ratio of 0.002). Activity nevertheless emerged in broth microdilution, where close solid–cell contact is possible, including for pristine HAp and for LTA@HAp. This pattern indicates that contact-dependent processes (physical adsorption of cells onto the composite and direct surface effects) dominate over classical diffusive ion-release killing under these conditions, although a contribution from short-range ion release at the particle–cell interface cannot be excluded.

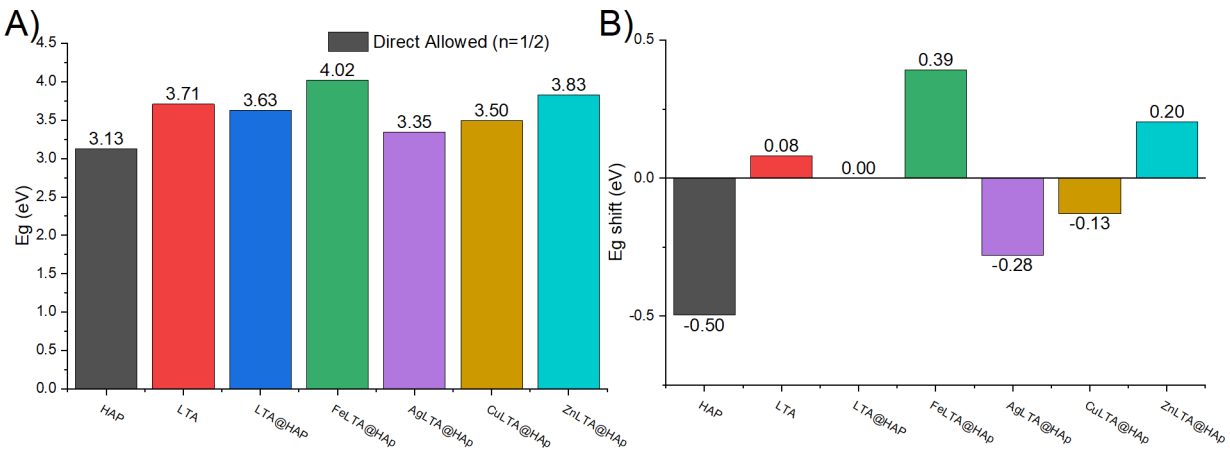

Figure 5: (A) Bandgap energy (E_g) values and corresponding (B) bandgap shifts for HAp, LTA, LTA@HAp, AgLTA@HAp, ZnLTA@HAp, FeLTA@HAp, and CuLTA@HAp, calculated from the direct allowed transition model (n = 1/2).

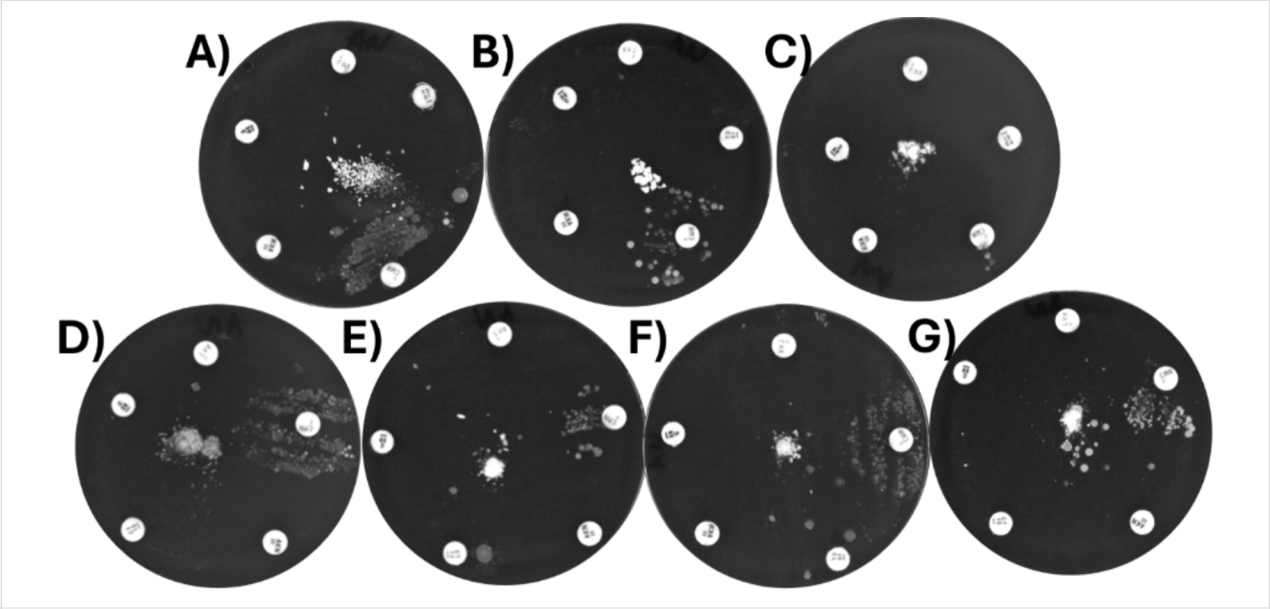

Figure 6: Antimicrobial activity comparison of antibiotics and the powder of (A) HAp, (B) LTA, (C) LTA@HAp, (D) AgLTA@HAp, (E) ZnLTA@HAp, (F) FeLTA@HAp, and (G) CuLTA@HAp evaluated by the agar diffusion method against a mouth swab.

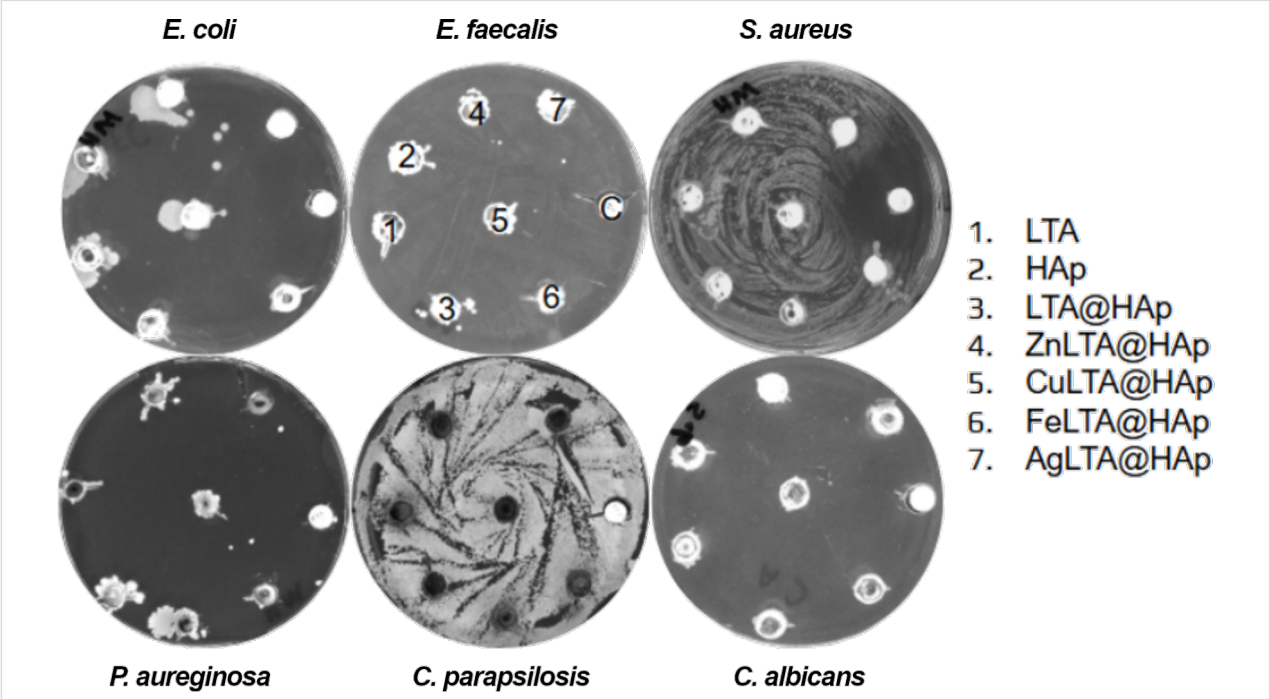

Figure 7: Antimicrobial activity of LTA, HAp, LTA@HAp, ZnLTA@HAp, CuLTA@HAp, FeLTA@HAp, and AgLTA@HAp evaluated by the agar diffusion method against *E. coli*, *E. faecalis*, *S. aureus*, *P. aeruginosa*, *C. parapsilosis*, and *C. albicans*.

In the broth microdilution assays (Figure 8), particles and cells remain in close and continuous contact. Under these conditions, all materials reduced metabolic activity, including the metal-free ones (LTA, HAp, and LTA@HAp). The reduction in metabolic activity can therefore not be attributed to the metals alone, which suggests that the composite architecture itself contributes to microbial inhibition. This contrasts with the agar diffusion assay, in which no inhibition zones formed, and agrees with our previous observations on LTA [34], where growth inhibition emerged in broth because the greater particle mobility increased the frequency of particle–cell interactions. Several processes may therefore contribute, such as adsorption

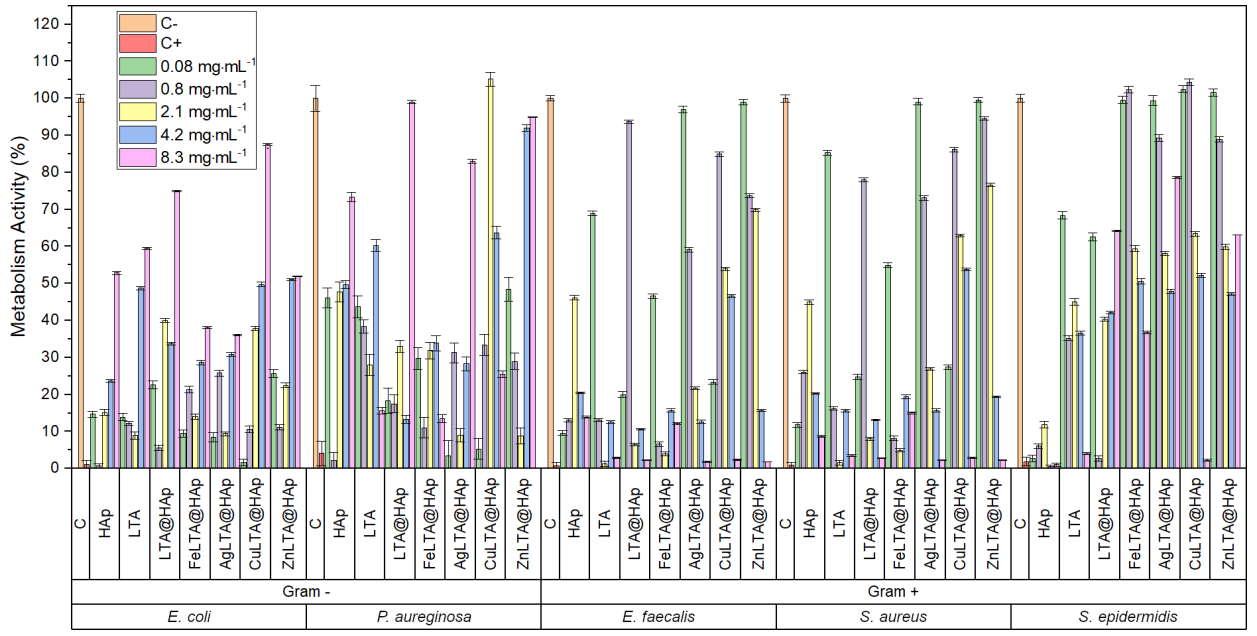

Figure 8: Metabolism activity (%) measured in a micro broth assay by the fluorescence intensity of resazurin with an excitation of 560 nm and emission at 590 nm after the incubation of *P. aeruginosa*, *E. faecalis*, *E. coli*, and *S. aureus* to assess the concentration-dependent effect of the materials (LTA, HAp, LTA@HAp, AgLTA@HAp, ZnLTA@HAp, FeLTA@HAp, and CuLTA@HAp) at final well concentrations of 0.08, 0.8, 2.1, 4.2, and 8.3 mg·mL^{-1}.

of cells onto the zeolite or HAp surface, ROS-related processes, and interactions with metal ions at the particle–cell interface [35].

Since resazurin reduction does not discriminate among these processes, the shape of the concentration–response profile was used as an indicator of the dominant process, as applied previously to a zeolite system [35]. A monotonic profile is attributed to the adsorption of cells onto the composite: The adsorbed cells are sequestered from the nutrient medium, which reduces metabolic activity without requiring a chemically toxic mechanism. A non-monotonic profile, in contrast, indicates that more than one process operates simultaneously, with adsorption competing with contact-mediated effects at the particle surface, such as ROS generation and metal interactions.

These categories describe the dominant behavior of each material–strain combination. Under this criterion, the metal-free materials already showed strain-dependent behavior. HAp contains no exchangeable metals, which excludes metal-ion release, yet its profiles were complex, with maximum inhibition at 0.8 mg·mL^{-1} for the Gram-negative strains (U-shaped profile) and at 0.08 and 8.3 mg·mL^{-1} for the Gram-positive strains (inverted U-shaped profile), which means that more than one process contributes to the inhibition for this sample. Pristine LTA also showed complex, non-monotonic profiles for both Gram-negative and Gram-positive bacteria. Combining the two materials (LTA@HAp) produced a clearer Gram-dependent split relative to pristine LTA [34], with greater inhibition of Gram-negative bacteria at the lower material concentrations and the opposite behavior for Gram-positive bacteria, which were inhibited more strongly at the higher concentrations. This is consistent with the role of the cell envelope: The peptidoglycan-rich Gram-positive wall and the lipopolysaccharide-rich Gram-negative outer membrane differ in surface charge, which modulates their electrostatic affinity for the particle surface [36]. The ANOVA showed a significant interaction between Gram type and final well concentration ($p < 0.1$), supporting a relationship between the inhibitory effect of the particles and the surface charge of the bacteria (Figure 9A).

The materials also produced a significant change in metabolic activity ($p < 0.05$) with the same Gram-dependent split (Figure 9B). The metal-free materials gave partial inhibition (metabolic activity < 50%) for both Gram-positive and Gram-negative bacteria, in the order HAp > LTA > LTA@HAp. These metal-free materials inhibited Gram-positive bacteria slightly more strongly, a trend that was reversed by the incorporation of the metals, which increased the inhibition of Gram-negative bacteria. The same order was nevertheless observed for both Gram types, FeLTA@HAp > AgLTA@HAp > CuLTA@HAp > ZnLTA@HAp, with FeLTA@HAp being the most effective against Gram-positive bacteria and HAp the most effective against Gram-negative bacteria.

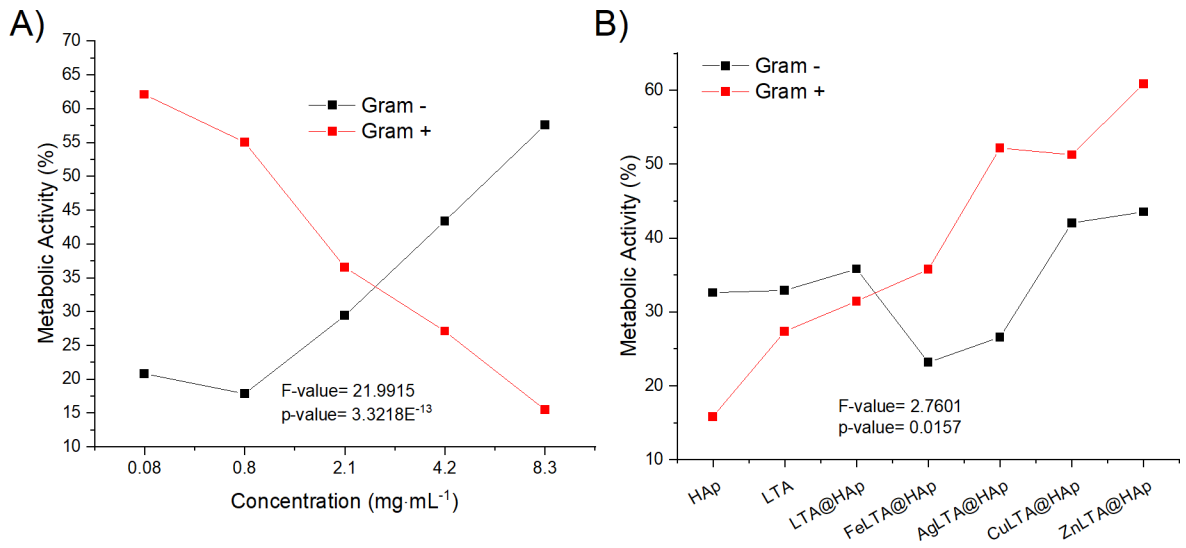

Figure 9: Means comparison plots from an ANOVA for bacterial metabolic activity (%) and the interaction effect between (A) Gram-type bacteria (Gram– and Gram+) and material concentration (final well concentrations of 0.08, 0.8, 2.1, 4.2, and 8.3 mg·mL^{-1}) and (B) distributed by material (LTA, HAp, LTA@HAp, AgLTA@HAp, ZnLTA@HAp, FeLTA@HAp, and CuLTA@HAp).

Although no new crystalline phase or detectable change in surface composition can explain the differences among the metal-modified composites, a significant difference was found between metabolic activity and the material used ($p < 0.01$; Figure 10A). Among the metal-functionalized composites, FeLTA@HAp performed best, achieving the highest overall inhibition of metabolic activity. Its profile for both Gram types (Figure 10B) corresponds to a partial metabolic inhibitor at all concentrations, except at 0.8 mg·mL^{-1} for the Gram-positive strains. This activity is plausibly linked to the redox-active nature of the iron species, which may promote Fenton-like reactions that generate ROS on contact with the bacterial cells [12,37].

AgLTA@HAp, ZnLTA@HAp, and CuLTA@HAp also increased the inhibition of metabolic activity at specific concen-

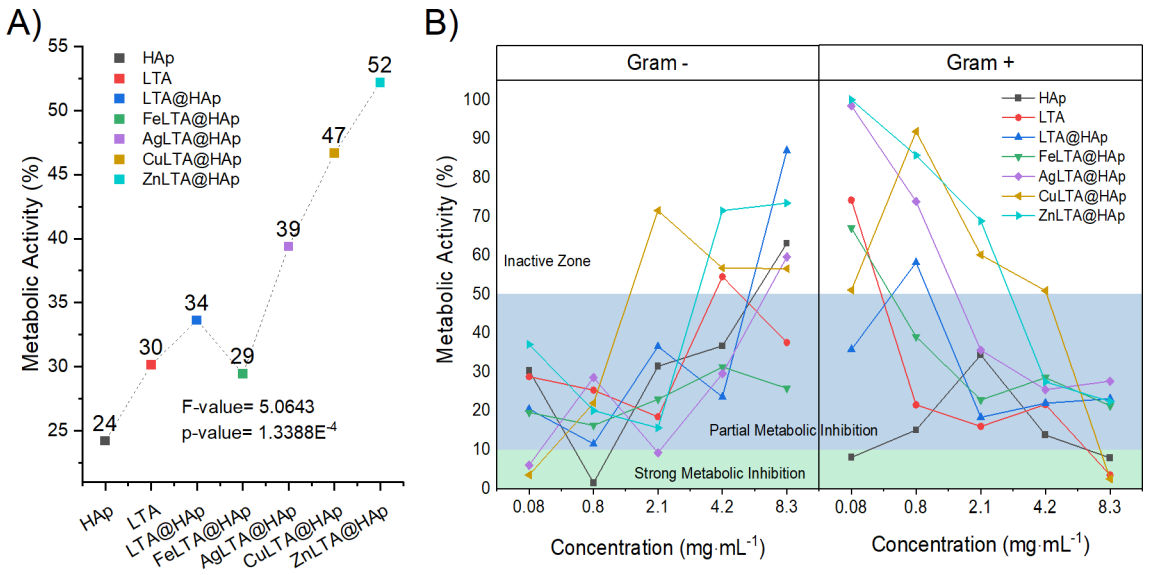

Figure 10: Means comparison plots from an ANOVA for bacterial metabolic activity (%), (A) distributed by material (LTA, HAp, LTA@HAp, AgLTA@HAp, ZnLTA@HAp, FeLTA@HAp, and CuLTA@HAp) and the effect with (B) Gram-type bacteria (Gram– and Gram+) and concentration (final well concentrations of 0.08, 0.8, 2.1, 4.2, and 8.3 mg·mL^{-1}).

trations (Figure 10B). AgLTA@HAp was a strong metabolic inhibitor at 0.08 mg·mL^{-1} for the Gram-negative strains and a partial inhibitor for the Gram-positive strains at concentrations above 2.1 mg·mL^{-1}. CuLTA@HAp showed the same inverse behavior, acting as a strong inhibitor of Gram-negative bacteria at the lowest concentration (0.08 mg·mL^{-1}) and of Gram-positive bacteria at the highest one (8.3 mg·mL^{-1}). ZnLTA@HAp behaved as a partial inhibitor for both Gram types, again with greater inhibition of Gram-negative bacteria at low concentrations and of Gram-positive bacteria at high concentrations. Although the metal contents were below the detection limits of XRD and EDS, the metals appear to modulate the magnitude of the inhibition rather than to change the dominant process set by the support. The profile of each sample is complex, but the same Gram-dependent trend is observed throughout: Gram-negative bacteria are inhibited mainly at low concentrations and Gram-positive bacteria at high concentrations. This suggests that even a small amount of metal alters the particle–cell interface, possibly through a change in surface charge, and that at high particle concentrations the thick peptidoglycan layer of Gram-positive bacteria no longer protects the cell from the particles [38]. Further work is required to describe the inhibition of metabolism by these composites. Gram-positive bacteria generally appeared more susceptible at high concentrations, whereas the effects against Gram-negative strains were more variable and were usually observed at low concentrations. Overall, the dominant behavior depended on the target organism and surface interactions rather than on diffusible species governed the inhibition under the conditions tested [39]. Direct confirmation will require measurements of metal release, viable-cell counts, ROS probes, and zeta-potential measurements.

Given the successful preparation route and the Gram-dependent inhibition of metabolic activity, these sonochemically prepared metal-functionalized LTA zeolite/hydroxyapatite composites are candidates for further study. The combined characterization confirmed that the LTA framework is preserved and that dispersed metal species are incorporated without the formation of segregated crystalline phases. These findings indicate that metal speciation and surface distribution are important for the antimicrobial behavior of zeolite-based composites, and the sonochemical route proved effective for dispersing the metals while maintaining the structural integrity of the composite.

Some limitations of this study should be acknowledged. The metal loading was low (nominal molar ratio 0.002), which may explain the moderate activity observed under some conditions. The antimicrobial evaluation was restricted to planktonic bacteria, whereas biofilm models are clinically relevant for implant-associated infections and should be the subject of further work on these materials. Cytotoxicity towards mammalian cells and the long-term stability of the composites in simulated biological fluids also remain to be established before biomedical applications can be considered.

Future work includes the systematic optimization of the metal and HAp loadings, the exploration of synergistic metal combinations, and surface-modification strategies to enhance contact-mediated efficiency. In vivo studies would be needed to confirm any combined regenerative and antimicrobial performance of these materials as coatings for orthopedic and dental implants [8]. Overall, the results identify metal-functionalized LTA/HAp composites, particularly those containing iron, as candidates for further development of infection-resistant biomaterials [40].

Conclusion

This preliminary study demonstrated the synthesis of metal-functionalized LTA zeolite/hydroxyapatite composites by a sonochemically assisted ion-exchange method. The characterization did not detect the Ag, Zn, Fe, and Cu species, consistent with their low content and high dispersion, and no crystalline metal or oxide phases were formed. Distinct localization states are proposed (surface clusters for Ag, surface ions for Zn, and cationic exchange sites for Fe and Cu) on the basis of the small changes detected by UV–vis spectroscopy, which were correlated with the optical bandgap and with the inhibition of metabolic activity. The materials inhibited metabolic activity in a Gram-dependent manner, being more effective against Gram-positive bacteria at the higher material concentrations and against Gram-negative bacteria at the lower ones. Among the metal-containing compositions, FeLTA@HAp gave the most consistent inhibition, acting as a partial inhibitor for both Gram-negative and Gram-positive bacteria at a relatively low concentration (0.8 mg·mL^{-1}). Pristine HAp and the metal-free LTA@HAp composite also inhibited the metabolic activity of Gram-negative bacteria appreciably, which underlines the contribution of the composite architecture itself. The broth assays further showed that these materials, particularly when loaded with Ag, Zn, Fe, or Cu, can be tuned to inhibit the metabolic activity of Gram-positive bacteria, with a marked dependence on the material concentration. These results highlight the importance of metal incorporation, surface distribution, and composite design in the development of contact-active biomaterials. The platform combines the known osteoconductive properties of hydroxyapatite with the ion-exchange versatility of the LTA zeolite and is a promising basis for studies on infection-resistant bone grafts and implants.

Acknowledgements

The authors acknowledge the support provided and access to its equipment and infrastructure of the: Programa Universitario de Prevención de Infecciones (UABC), Laboratorio de

Investigación Epidemiológica (UABC); Unidad de Laboratorio Comunitario y Diagnóstico Molecular Universitario (UABC) and Albergue Las Memorias. Jesús Isaías de León Ramírez, gratefully acknowledges the postdoctoral fellowship provided by SECIHTI (BP-PM-20250912153102760-13358161). Likewise, Victor Alfredo Reyes-Villegas acknowledges that this work was supported by Universidad Nacional Autónoma de México Postdoctoral Program, hosted at the Instituto de Investigación en Materiales (IIM).

Funding

This work was financially supported by UNAM (National Autonomous University of Mexico) through supercomputer time in the LANCAD-UNAM-DGTIC-423 and 084 projects, as well as resources provided in the project SECIHTI CBF-2025-G-470.

Author Contributions

Jesús Isaías De León-Ramírez: conceptualization; data curation; investigation; methodology; visualization; writing – original draft. José Román Chávez-Méndez: funding acquisition; investigation; methodology; project administration. Sergio Pérez-Sicairos: project administration; resources; supervision; validation. Lizzett López-Yee: resources; writing – review & editing. Vitalii Petranovskii: data curation; funding acquisition; methodology; resources; supervision. Víctor Alfredo Reyes-Villegas: conceptualization; data curation; formal analysis; investigation; methodology; software; visualization; writing – original draft; writing – review & editing.

ORCID® iDs

Jesús Isaías De León-Ramírez - https://orcid.org/0000-0003-1393-610X
José Román Chávez-Méndez - https://orcid.org/0000-0002-0445-7601
Sergio Pérez-Sicairos - https://orcid.org/0000-0002-1244-3015
Vitalii Petranovskii - https://orcid.org/0000-0002-8794-0593

Data Availability Statement

Data generated and analyzed during this study is available from the corresponding author upon reasonable request.

References

1. Shinde, A.; Mohan, A.; Bulusu, V. M.; Soni, P.; Singh, J.; Khadanga, S.; Joshi, A.; Venkatachalapathy, P.; Kanwar, R. K.; Miraj, S. S.; Munisamy, M. *Front. Antibiot.* **2026,** *5,* 1632790. doi:10.3389/frabi.2026.1632790
2. Chen, W.; Zeng, Y.; Zheng, J.; Wang, J.; Gu, W.; Li, M.; Cheng, Z.; Qian, J.; Zhang, X.; Kabali, E.; Lv, C.; Chen, Y.; Yang, G.; Zhou, N.; Tan, X.; Zhu, C.; Tun, H. M.; Mohsin, M.; Rahman, T.; Zhou, Z.; Xiao, Y.; Chen, H.; Shi, C.; Bergquist, R.; Ross Fitzgerald, J.; Chen, S.; Chang, Y.-F.; Wang, Z.; Zhou, X.; Guo, X.; Utzinger, J.; Song, J.; Zhu, Y. *Nat. Med.* **2026,** *32,* 1362–1373. doi:10.1038/s41591-026-04257-1
3. Hojda, S.; Biegun-Żurowska, M.; Skórkowska, A.; Klesiewicz, K.; Ziąbka, M. *Int. J. Mol. Sci.* **2025,** *26,* 1646. doi:10.3390/ijms26041646
4. Yu, Z.; Wang, Z.; Chen, Y.; Wang, Y.; Tang, L.; Xi, Y.; Lai, K.; Zhang, Q.; Li, S.; Xu, D.; Tian, A.; Wu, M.; Wang, Y.; Yang, G.; Gao, C.; Huang, T. *Biomaterials* **2025,** *313,* 122772. doi:10.1016/j.biomaterials.2024.122772
5. Sokić, K.; Dikić, J.; Veljović, Đ.; Jelić, I.; Radovanović, D.; Štulović, M.; Jevtić, S. *Processes* **2025,** *13,* 818. doi:10.3390/pr13030818
6. Zarrintaj, P.; Mahmodi, G.; Manouchehri, S.; Mashhadzadeh, A. H.; Khodadadi, M.; Servatan, M.; Ganjali, M. R.; Azambre, B.; Kim, S.-J.; Ramsey, J. D.; Habibzadeh, S.; Saeb, M. R.; Mozafari, M. *MedComm* **2020,** *1,* 5–34. doi:10.1002/mco2.5
7. Faraji, D.; Jahandideh, A.; Asghari, A.; Akbarzadeh, A.; Hesaraki, S. *Arch. Razi Inst.* **2019,** *74,* 395–403. doi:10.22092/ari.2018.121308.1211
8. Purnomo, P.; Setyarini, P.; Riyadi, T.; Sulistyaningsih, D. *FME Transactions* **2020,** *48,* 522–531. doi:10.5937/fme2003522s
9. Tawiah, P. O.; Gaessler, L. F.; Anderson, G. M.; Oladokun, E. P.; Dahl, J.-U. *mSphere* **2025,** *10,* e00017-25. doi:10.1128/msphere.00017-25
10. Bowden, L. C.; Sithole, S. T.; Walton, E. C.; Han Chen, J.; Sorensen, J. J.; Bowden, A. E.; Jensen, B. D.; Berges, B. K. *Appl. Environ. Microbiol.* **2025,** *91,* e01053-25. doi:10.1128/aem.01053-25
11. Pino, P.; Bosco, F.; Mollea, C.; Onida, B. *Pharmaceutics* **2023,** *15,* 970. doi:10.3390/pharmaceutics15030970
12. Tasnim, N. T.; Ferdous, N.; Rumon, M. M. H.; Shakil, M. S. *ACS Omega* **2024,** *9,* 16–32. doi:10.1021/acsomega.3c06323
13. Kubota, M.; Nakabayashi, T.; Matsumoto, Y.; Shiomi, T.; Yamada, Y.; Ino, K.; Yamanokuchi, H.; Matsui, M.; Tsunoda, T.; Mizukami, F.; Sakaguchi, K. *Colloids Surf., B* **2008,** *64,* 88–97. doi:10.1016/j.colsurfb.2008.01.012
14. Watanabe, Y.; Ikoma, T.; Suetsugu, Y.; Yamada, H.; Tamura, K.; Komatsu, Y.; Tanaka, J.; Moriyoshi, Y. *J. Eur. Ceram. Soc.* **2006,** *26,* 469–474. doi:10.1016/j.jeurceramsoc.2005.07.024
15. Xiao, H.; Du, J.; Shen, T.; Hu, Y.; Zhang, Y.; Yan, Z.; Shan, Y.; Shan, W.; Yan, Y.; Yu, Y.; He, H. *Appl. Catal., B* **2026,** *384,* 126218. doi:10.1016/j.apcatb.2025.126218
16. Amari, S.; Boshrouyeh, R.; Darestani, M. *3 Biotech* **2026,** *16,* 278. doi:10.1007/s13205-026-04863-3
17. Ramirez, J. I. D. L.; Reyes-Villegas, V. A.; Sicairos, S. P.; Chávez-Méndez, J. R.; Pérez-Cabrera, L.; Torres, V. G.; González Crisóstomo, J. C.; Zavala-Flores, E.; Murrieta-Rico, F. N.; Petranovskii, V. Ultrasonic Coating of LTA Zeolites by Antibacterial and Antibiofilm Nanoparticles. In *Advancements in Zeolites and Micro-Meso Porous Hierarchical Materials;* Murrieta-Rico, F.; Antúnez-García, J.; Petranovskii, V., Eds.; IGI Global Scientific Publishing, 2025; pp 395–426. doi:10.4018/979-8-3373-0320-8.ch011
18. De León-Ramírez, J. I.; Reyes Villegas, V. A.; Pérez-Sicairos, S.; Chávez Méndez, J. R.; Chávez-Rivas, F.; Yocupicio-Gaxiola, R. I.; Petranovskii, V. *PLoS One* **2025,** *20,* e0324997. doi:10.1371/journal.pone.0324997
19. LTA Linde Type A Si(50), Al(50). In *Verified Syntheses of Zeolitic Materials;* Robson, H.; Lillerud, K. P., Eds.; Elsevier, 2001; pp 179–181. doi:10.1016/b978-044450703-7/50153-8
20. LeGeros, R. Z. Calcium Phosphates in Oral Biology and Medicine. *Monographs in Oral Science;* 1991; Vol. 15. doi:10.1159/isbn.978-3-318-04021-0

21. Nyankson, E.; Efavi, J. K.; Yaya, A.; Manu, G.; Asare, K.; Daafuor, J.; Abrokwah, R. Y. *Cogent Eng.* **2018,** *5,* 1440480. doi:10.1080/23311916.2018.1440480
22. Jiraroj, D.; Tungasmita, S.; Tungasmita, D. N. *Powder Technol.* **2014,** *264,* 418–422. doi:10.1016/j.powtec.2014.05.049
23. Shannon, R. D. *Acta Crystallogr., Sect. A* **1976,** *32,* 751–767. doi:10.1107/s0567739476001551
24. Che Hashim, N.; Nordin, D. *Mater. Today: Proc.* **2019,** *19,* 1562–1571. doi:10.1016/j.matpr.2019.11.184
25. Dorozhkin, S. V. *Acta Biomater.* **2014,** *10,* 2919–2934. doi:10.1016/j.actbio.2014.02.026
26. Ain, Q.-u.; Munir, H.; Jelani, F.; Anjum, F.; Bilal, M. *Mater. Res. Express* **2020,** *6,* 125426. doi:10.1088/2053-1591/ab715d
27. Linnert, T.; Mulvaney, P.; Henglein, A. *J. Phys. Chem.* **1993,** *97,* 679–682. doi:10.1021/j100105a024
28. Grandjean, D.; Coutiño-Gonzalez, E.; Cuong, N. T.; Fron, E.; Baekelant, W.; Aghakhani, S.; Schlexer, P.; D'Acapito, F.; Banerjee, D.; Roeffaers, M. B. J.; Nguyen, M. T.; Hofkens, J.; Lievens, P. *Science* **2018,** *361,* 686–690. doi:10.1126/science.aaq1308
29. Bols, M. L.; Ma, J.; Rammal, F.; Plessers, D.; Wu, X.; Navarro-Jaén, S.; Heyer, A. J.; Sels, B. F.; Solomon, E. I.; Schoonheydt, R. A. *Chem. Rev.* **2024,** *124,* 2352–2418. doi:10.1021/acs.chemrev.3c00602
30. Chen, J.; Huang, W.; Bao, S.; Zhang, W.; Liang, T.; Zheng, S.; Yi, L.; Guo, L.; Wu, X. *RSC Adv.* **2022,** *12,* 27746–27765. doi:10.1039/d2ra05107a
31. Piccirillo, C.; Castro, P. M. L. *J. Environ. Manage.* **2017,** *193,* 79–91. doi:10.1016/j.jenvman.2017.01.071
32. Rajendran, S.; Khan, M. M.; Gracia, F.; Qin, J.; Gupta, V. K.; Arumainathan, S. *Sci. Rep.* **2016,** *6,* 31641. doi:10.1038/srep31641
33. Pelaez, M.; Nolan, N. T.; Pillai, S. C.; Seery, M. K.; Falaras, P.; Kontos, A. G.; Dunlop, P. S. M.; Hamilton, J. W. J.; Byrne, J. A.; O'Shea, K.; Entezari, M. H.; Dionysiou, D. D. *Appl. Catal., B* **2012,** *125,* 331–349. doi:10.1016/j.apcatb.2012.05.036
34. De León Ramirez, J. I.; Reyes Villegas, V. A.; Cadena-Nava, R. D.; Loredo-Garcia, E.; Chávez-Rivas, F.; González-Torres, V.; Petranovskii, V. *Microporous Mesoporous Mater.* **2024,** *380,* 113295. doi:10.1016/j.micromeso.2024.113295
35. González-Crisostomo, J. C.; López-Juárez, R.; Zavala-Flores, E.; Villegas-Chávez, J. L.; Candolfi-Arballo, O.; Reyes Villegas, V. A.; Ramírez, J. I. D. L.; Petranovskii, V. *PLoS One* **2026,** *21,* e0344459. doi:10.1371/journal.pone.0344459
36. Belaabed, R.; Elabed, S.; Addaou, A.; Laajab, A.; Rodríguez, M. A.; Lahsini, A. *Bol. Soc. Esp. Ceram. Vidrio* **2016,** *55,* 152–158. doi:10.1016/j.bsecv.2016.05.001
37. Chen, S.; Popovich, J.; Zhang, W.; Ganser, C.; Haydel, S. E.; Seo, D.-K. *RSC Adv.* **2018,** *8,* 37949–37957. doi:10.1039/c8ra06556j
38. Slavin, Y. N.; Asnis, J.; Häfeli, U. O.; Bach, H. J. *NanoBiotechnology* **2017,** *15,* 65. doi:10.1186/s12951-017-0308-z
39. Vimbela, G.; Ngo, S. M.; Fraze, C.; Yang, L.; Stout, D. A. *Int. J. Nanomed.* **2017,** *12,* 3941–3965. doi:10.2147/ijn.s134526
40. Xiang, B.; Jiang, J.; Wang, H.; Song, L. *Front. Bioeng. Biotechnol.* **2025,** *13,* 1586898. doi:10.3389/fbioe.2025.1586898

License and Terms

This is an open access article licensed under the terms of the Beilstein-Institut Open Access License Agreement (https://www.beilstein-journals.org/bjnano/terms), which is identical to the Creative Commons Attribution 4.0 International License (https://creativecommons.org/licenses/by/4.0). The reuse of material under this license requires that the author(s), source and license are credited. Third-party material in this article could be subject to other licenses (typically indicated in the credit line), and in this case, users are required to obtain permission from the license holder to reuse the material.

The definitive version of this article is the electronic one which can be found at:
https://doi.org/10.3762/bjnano.17.114